Southern Ocean temperature records and ice-sheet models demonstrate rapid Antarctic ice sheet retreat under low atmospheric CO2 during Marine Isotope Stage 31

Catherine Beltran, Nicholas R. Golledge, Christian Ohneiser, Douglas E. Kowalewski, Marie-Alexandrine Sicre, Kimberly J. Hageman, Robert Smith, Gary S. Wilson, François Mainié

Southern Ocean temperature records and ice-sheet models demonstrate rapid Antarctic ice sheet retreat under low atmospheric CO_2 during Marine Isotope Stage 31.

*Beltran Catherine[1], Golledge Nicholas R.[2,3], Ohneiser Christian[4], Kowalewski Douglas E.[5], Sicre Marie-Alexandrine[6], Hageman Kimberly J.[7], Smith Robert[1], Wilson Gary S.[1], Mainié François[6].

1. Department of Marine Science, University of Otago, PO Box 56, Dunedin 9054, New Zealand
catherine.beltran@otago.ac.nz
2. Antarctic Research Centre, Victoria University of Wellington, Wellington 6140, New Zealand
3. GNS Science, Avalon, Lower Hutt 5011, New Zealand
4. Department of Geology, University of Otago, PO Box 56, Dunedin 9054, New Zealand
5. Department of Earth, Environment, and Physics, Worcester State University, Worcester, Massachusetts 01602, USA
6. Sorbonne Universités (UPMC, Univ. Paris 06)-CNRS-IRD-MNHN, LOCEAN Laboratory, 4 Place Jussieu, F-75005 Paris, France.
7. Department of Chemistry, University of Otago, PO Box 56, Dunedin 9054, New Zealand

Highlights

- We quantify precisely the magnitude of ocean warming using the **first ever** Southern Ocean molecular paleo-temperature reconstructions during the warm Marine Isotope Stage 31 (MIS31- 1.085 and 1.055 million years ago).
- Our data show a sustained surface Southern Ocean warming and a collapse of the Antarctic and sub Antarctic ocean fronts during that warm period and under low atmospheric CO_2 concentrations.
- We use sea surface temperature reconstructions to test the scenarios for the AIS retreat during MIS31 using coupled ice-sheet/ice-shelf model.
- We propose a two-step model for deglaciating West Antarctica which involves mild ocean warming (a new temperature threshold) which forces ice margin retreat followed by rapid ocean warming as the ice sheet retreats.
- Our work shows that the Paris Agreement target temperature of 1.5°C is sufficient to drive runaway retreat of the West Antarctic Ice Sheet. We derive this conclusion from the robust, ocean temperature proxy record and ice sheet simulation.

Abstract

Over the last 5 million years, the Earth's climate has oscillated between warm (interglacial) and cold (glacial) states. Some particularly warm interglacial periods (i.e. 'super-interglacials') occurred under low atmospheric CO_2 and may have featured extensive Antarctic ice sheet collapse. Here we focus on an extreme super-interglacial known as Marine Isotope Stage 31 (MIS31), between 1.085 and 1.055 million years ago and is the subject of intense discussion. We reconstructed the first Southern Ocean and Antarctic margin sea surface temperatures (SSTs) from organic biomarkers and used them to constrain numerical ice sheet-shelf simulations. Our SSTs indicate that the ocean was on average 5 °C (±1.2 °C) warmer in summer than today between 50 °S and the Antarctic ice margin. Our most conservative ice sheet simulation indicates a complete collapse of the West Antarctic Ice Sheet (WAIS) with additional deflation of the East Antarctic Ice Sheet. We suggest the WAIS retreated because of anomalously high Southern Hemisphere insolation coupled with the intrusion of Circumpolar Deep Water onto the continental shelf under poleward-intensified winds leading to a shorter sea ice season and ocean warming at the continental margin. In this scenario, the extreme warming we observed likely reflects the extensively modified oceanic and hydrologic system following ice sheet collapse. Our work highlights the sensitivity of the Antarctic ice sheets to minor oceanic perturbations that could also be at play for future changes.

Keywords

Super-interglacial, Pleistocene, Paleoceanography, Paleoclimate modeling, Antarctica, Southern Ocean, Organic Geochemistry

1. Introduction

Some geological records suggest that during the early Pleistocene Marine Isotope Stage 31 (MIS31 ~1.08 to 1.06 Ma), under preindustrial atmospheric CO_2 conditions (Lüthi et al. 2008; Hönisch et al., 2009), global mean sea level rose by ~20 m (Raymo et al., 2006). Recent climate simulations estimate that the global mean temperature increased by 1.2 ^{o}C during boreal summers in the Northern Hemisphere (Justino et al., 2019). The magnitude of the sea level high stand and geological evidence suggest a major retreat of the West Antarctic Ice Sheet (WAIS), part of the East Antarctic Ice Sheet (EAIS) and probably also the Greenland Ice Sheet (Hearty et al., 1999; Raymo et al., 2006; Dutton and Lambeck, 2012; Dutton et al., 2015) during this time. In sediment drill core records from around Antarctica, MIS31 is identified by the abrupt appearance of foraminiferal oozes and coccolith-bearing sediments in the Weddell Sea and Prydz Bay and of bioclastic limestone in the Ross Sea (Bohaty et al., 1998; Scherer et al., 2003; Villa and Wise, 1998; Villa et al., 2008; Villa et al., 2012). This indicates a significant southward migration of the Polar Front (PF), surface ocean warming and open-marine conditions in the Ross and Weddell Seas, with a reduction in sea ice extent relative to the present day (Becquey and Gersonde, 2002; Scherer et al., 2008; Winter et al., 2010; Martinez-Garcia et al., 2010; McKay et al., 2012). To date, elevated ocean surface temperatures have been inferred from paleoecological and sedimentological changes observed in sediment cores around the Antarctic margin (Bohaty et al., 1998; Scherer et al., 2003; 2008; Winter et al., 2010; Dunbar, 2012; Teitler et al., 2005). However, the scarcity of precise surface ocean temperature data has so far limited models from realistically simulating the ice sheet and Southern Ocean responses during MIS31 (Supplementary Information Section 1). Consequently, it has also not been possible to isolate the cause of ice melt and sea

level rise although an unusual orbital configuration and elevated polar summer insolation have been implicated (Laskar et al., 2004; Scherer et al., 2008).

Ice-sheet/ice-shelf and global climate simulations have highlighted the prominent role the ocean plays in controlling the position of the grounding lines of the WAIS and portions of the EAIS (Jacobs et al., 1992; Dinniman et al., 2016). Here we generate the first SST time series from molecular paleothermometric methods (alkenone unsaturation index $U^{k'}_{37}$ - Prahl et al., 1988; and the Long Chain Diol Index LDI - Rampen et al., 2012) from Southern Ocean and Antarctic margin deep-sea sediment cores. We then use these sea surface temperature reconstructions to test the scenarios for the AIS retreat during MIS31 using coupled ice-sheet/ice-shelf model (Golledge, et al., 2015).

2. Material and Methods

2.1. Site locations and modern oceanography

To document the evolution of the sea surface temperatures (SST) in the Atlantic sector of the Southern Ocean during MIS31, we have selected the ODP Site 1094, situated approximately 2° south of the present Antarctic Polar Front (Schneider-Mor et al., 2008 - Fig. 1). To investigate the SSTs in the peri-Antarctic region, we have selected the IODP Site 1361 (Wilkes Land - Escutia et al., 2011) and the ODP Site 1101 (Antarctic Peninsula – Barker et al., 1999). We supplement our latitudinal temperature dataset with the high resolution alkenone-derived SSTs record from Martinez-Garcia et al. (2010) for the ODP Site 1090 situated North of the modern subantarctic front (SAF) and the Mg/Ca measurements on planktic foraminifera from the Cape Roberts Project Site 1 (CRP-1) drilled beneath the northwestern Ross Ice Shelf (Dunbar 2012 - Fig. 1). Sample sites were selected on the basis of previously reported occurrence of MIS31 sediments in the literature.

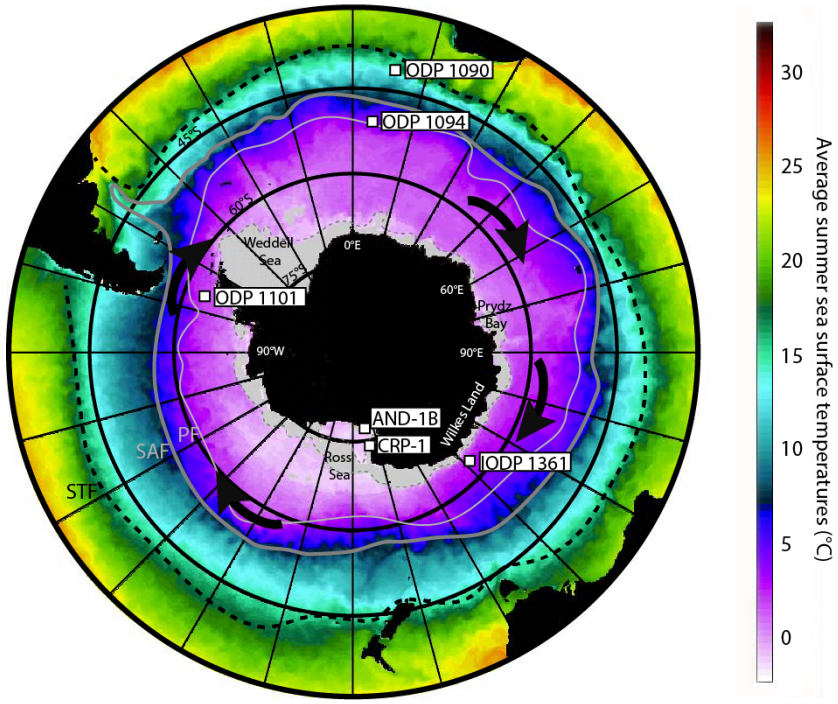

Figure 1: Location of the principal ocean frontal systems in the Southern Ocean (Orsi et al., 1995) and drill sites chosen for this study. The modern summer sea surface temperature map was modified after HYCOM Consortium for Data-Assimilative Ocean Modelling Southern Ocean Atlas (http://www7320.nrlssc.navy.mil/GLBhycom1-12/skill.html). The general path for the Antarctic Circumpolar Current (ACC) is shown with the black arrows (Orsi et al., 1995). STF: subtropical Front (black dashed)- SAF: Subantarctic Front (dark grey)- PF: Polar Front (light grey).

ODP Site 1090 (42°54.8'S, 8°53.9'E) was drilled on the southern flank of the Agulhas Ridge, at a water depth of 3699 m. It lies within the modern subantarctic waters between the subtropical (STF) and the subantarctic (SAF) fronts in the Atlantic sector of the Southern Ocean. The modern annual SST at this location is 10 °C (9 °C in July-September - 11 °C in January-March; Levitus, 1994). Pleistocene sediment consists of foraminiferal nannofossil ooze and foraminifer-bearing nannofossil ooze.

ODP Site 1094 (53°10.8'S, 5°7.8'E) is located south of the Polar Front, north of the Weddell Gyre (Antarctic Circumpolar Current (ACC) -boundary) and within the biogenic silica belt (Gersonde et al., 1999). The site is located close to Bouvet Island, in the ice-free Antarctic Zone, at 2807 m water depth. The investigated sediments

(1094D 11H to 13H) mainly consist of carbonate bearing diatom ooze, with varying amounts of foraminifera and nannofossils (between 20% and 45%). The mean annual SST in this area is 0.7 °C, with mean temperatures of 0.2 °C in winter and of 2.5 °C during austral summer (Levitus, 1994).

IODP Site U1361 (64.4°S, 143.88°E) is located on the Wilkes Land margin, on the eastern levee of the Jussieau sub-marine channel. The mean annual SST in this area is around 0 °C (Levitus, 1994). Sediments from 1361A-2H consist of silty clay and calcareous silty clay. Sediments from 1361A-3H are foraminifera-bearing silty clay and diatom-rich silty clay. The occurrence of calcareous nannofossils have been reported in section 5W. We focused on the interval comprised between 1361A-2H-6W and 1361A3H4W because in some discrete intervals planktonic foraminifers were abundant (from Sample 2H-CC contains >90%).

ODP Site 1101 (64.37°S, -70.26°E) is located on the continental rise, west of the Antarctic peninsula, 94 km offshore the shelf edge. The mean annual SST in this area is around 0 °C (Levitus, 1994). Between 1101A9H1W100 and 1101A10H3W117 the sediments consist of laminated clayey silts and foraminifera-bearing clayey silts containing well preserved calcareous nannofossils.

Cape Roberts Project Site 1 (CRP-1) (77.0°S, 163.8°E) was drilled on the continental shelf in the western Ross Sea near the Transantarctic Mountain belt. Previous studies (Scherer et al., 2008) have focused on the unusual early Pleistocene carbonate rich lithostratigraphic Unit 3.1 corresponding to the MIS31 interglacial. This unique interval contains laminated sediments with abundant diatoms, planktic foraminifera and thoracospherids (calcareous dinoflagellates - Scherer et al., 2008).

2.2. Age models

We developed a chronology for the IODP Site 1361 from new paleomagnetic measurements performed on u-channel samples at the University of Otago Paleomagnetic Research Facility (OPRF). Our LDI-derived SST data were then converted from depth to the time by linear interpolation between geomagnetic reversals. The alkenone-derived temperatures for the ODP Site 1094 and ODP Site 1101 were converted from depth to time using the chronologies from shipboard paleomagnetic data.

2.2.1. IODP Site 1361

U-channel samples were collected at the IODP Core Repository at Texas A&M University and shipped to the University of Otago's Paleomagnetic Research Facility (OPRF). U-channel samples were collected from the IODP Site 1361 archive half core to establish a more precise magnetostratigraphy. Archive half core sections were demagnetized in fields of 20 mT during the expedition to build an initial age model construction and core characterization. Magnetic moment measurements were made at 1 cm intervals using the 2G Enterprises pass-through superconducting rock magnetometer which is housed in a 150 nT magnetically shielded room. U-channels were demagnetized in alternating magnetic field increments of 5 mT between 20 mT and 50 mT, then at 60 mT, 70 mT and finally at 100 mT. Demagnetization data were analysed on orthogonal vector component plots using the PuffinPlot software (Lurcock and Wilson, 2012). Polarity was determined from principal component analyses (PCA, Kirschvink, 1980) of data between the 20 mT and c. 50 mT increments which we interpret is the primary depositional remanent magnetizations (DRM). PCAs were typically anchored to the origin with the exception of thin intervals which were offset from the origin where a high coercivity magnetisation prevents complete demagnetisation. Rock magnetic data of these intervals did not

reveal unusual changes in magnetic mineralogy therefore we suggest that strongly magnetised, high coercivity drop stones may be responsible for the offset origins.

Our new magnetostratigraphy does not change the correlation with the GPTS (Tauxe et al., 2012) but does result in more precise placement of reversal boundaries (Fig. 2). Our new magnetostratigraphy places the C1r.1r-C1r.1n (988 ka) boundary (at 17.77m ±0.03m, the C1r.1n-C1r.2r (1072 ka) at 19.02m ± 0.17m, the top and base of the Cobb Mt (1178–1215 ka, Channell, 2017) at 20.54m ±0.06m and 20.92m ±0.04m respectively (Fig. 2). The C1n-C1r.1r (781 ka) transition spans a core break between 8.1 m and 14.34 m (11.22 m mid-point) where the lower contact on core 2H is affected by coring disturbance and the C1r.2r-C2n (1778 ka) transition occurs at 32.33m ±0.025m (Tauxe et al., 2012).

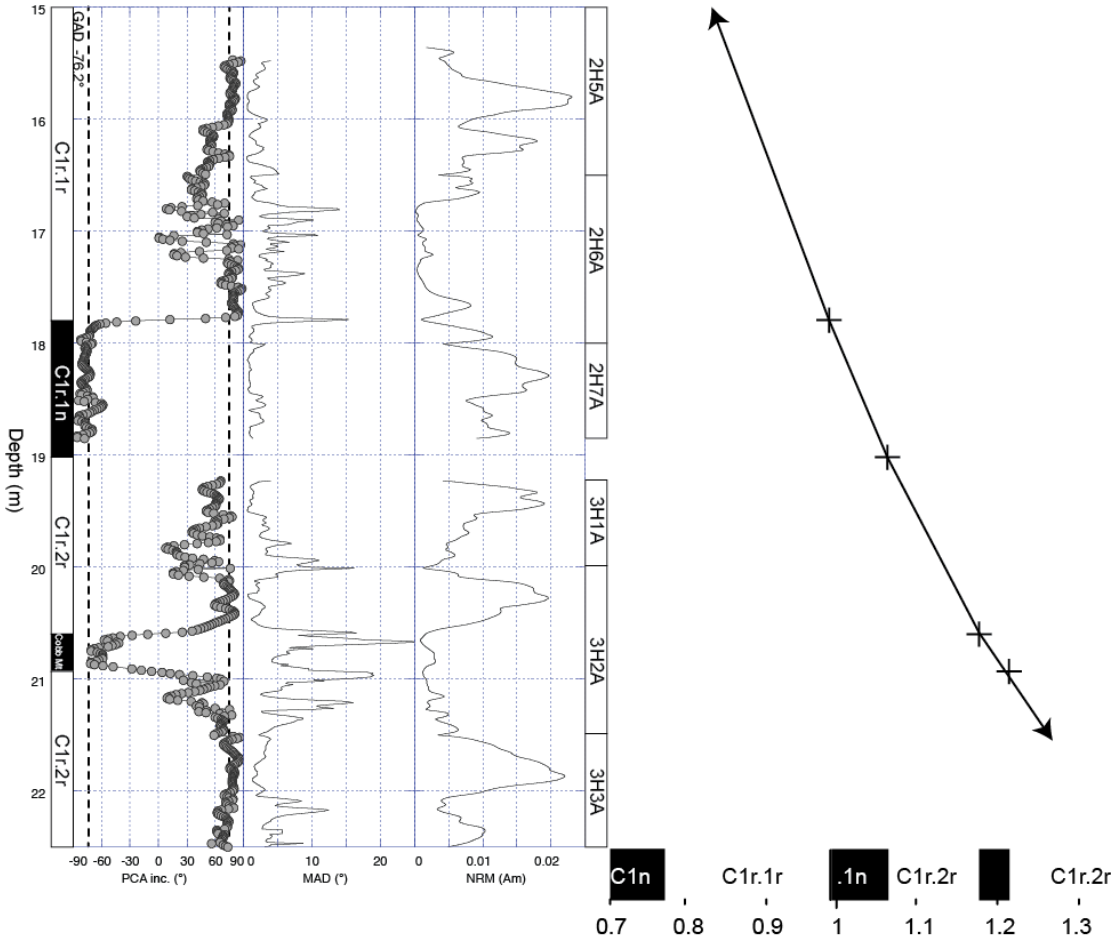

Figure 2: IODP 1361 age model developed in this study.

2.2.2. ODP Site 1094

196 The age model of ODP Site 1094A and 1094D was constructed from shipboard
197 paleomagnetic data where the 20 mT demagnetisation step was taken as the
198 characteristic remanent magnetisation as confirmed from complete laboratory
199 demagnetisation of u-channel samples (Channell and Stoner, 2002). The C1n-C1r.1r
200 boundary (781 ka) occurs at 99.61m, the C1r.1r-C1r.1n (988 ka) boundary at 123m
201 ±2.22m, the C1r.1n-C1r.2r (1072 ka) at 129m ± 0.38m, and the base of the Cobb Mt
202 (1178 ka) at 149.6 m.

203 **2.2.3. ODP Site 1101**

204 We adopted the age model (Acton et al., 2012) based on shipboard analyses and
205 shore-based laboratory analyses from u-channel samples. The C1n-C1r.1r (781 ka)
206 transition occurs at 55.05 m ±0.01 m, the C1r.1r-C1r.1n (988 ka) at 71.15 m ±0.19m,
207 the C1r.1n-C1r.2r (1072 ka) at 76.12m ± 0.17m, and the top and base of the Cobb Mt
208 (1178–1215 ka, Acton et al., 2012) at 81.61m ±0.65m and 82.53m ±0.01m
209 respectively.

2.3. Temperature reconstructions

To reconstruct the latitudinal SST gradient during the MIS31 super-interglacial along a transect from Sub-Antarctic to Antarctic water masses of the Southern Ocean, we used two complementary organic geochemical proxies for SSTs: the alkenone unsaturation ratio (Prahl et al., 1988 - $U^{k'}_{37}$) and the Long Chain Diol Index (Rampen et al., 2012 - LDI). The use of alkenone thermometry was motivated by the unusual presence of surface-dwelling calcareous nannofossils in 1 Ma-old sediments at extreme southern latitudes around the Antarctic (Scherer et al., 2008; Villa et al., 2005; 2007; 2012). Specifically, representatives belonging to the alkenone (long-chain unsaturated ketones) producer Noelarhabdaceae family (*Emiliania*, *Gephyrocapsa*, *Reticulofenetra*, *Pseudoemiliania*, *Dictyococcites* sp. – Marlowe et al., 1990; Beltran et al., 2007; 2011) were reported at drilling sites located south of the Polar Front (Fig. 1).

Although alkenones were detected at Site 1094 (concentrations between 2 and 25 ng/g), the concentrations were below detection limits at the Antarctic margin IODP Site U1361. Thus, we chose to use the long chain Diol Index (LDI) to reconstruct the SSTs at the Antarctic margin. This newly developed proxy for paleotemperatures (see Lopes dos Santos et al., 2013; de Bar et al., 2018), is based on the relative abundances of lipids with chain length of 28 and 30 carbon atoms containing two alcohol groups (long chain alkyl 1,13- and 1,15-diols; C_{28}1,13-diol, C_{30}1,13-diol and C_{30}1,15-diol). In the marine environment, these long chain diols have been found in diatoms and marine algae (Rampen et al., 2012). Although the source of the long chain diols is still under discussion, these molecules have existed at least since the Mesozoic era and are ubiquitous in the world ocean from the equator down to very high latitudes (74°S). The LDI index correlates best with temperature for modern water depths of 0 to 30 m

during the warmest months of the year.

Alkenone unsaturation ratios were measured on samples from ODP Site 1094D-11H-1W to 1094D-13H-3W (between 115.9 and 137.8 m) at a resolution of one sample every 30 cm (temporal resolution of 2.2 kyrs) and from ODP Site 1101A-9H-2W to 1101A-10H-4W (between 68.7 and 80.4 m) at a resolution of one sample every 45 cm (temporal resolution of 7.3 kyrs). For IODP Site 1361, we measured the Long chain diol index (LDI) on 12 samples from 1361A-2H-6W to 1361A-3H-3W (between 17.7 and 21.7 m) at a resolution of one sample every 35 cm (temporal resolution of 23 kyrs). We found Long chain diols in 10 samples. For both methods, sediment samples (6 to 9 g) were freeze-dried, homogenized, and extracted using an automated solvent extractor a Dionex 300 Accelerated Solvent Extractor with dichloromethane and methanol (9:1, v/v) at 1500 psi and 100°C to obtain a total lipid extract.

Alkenones were isolated by silica gel chromatography using solvents of increasing polarity following the procedure of Sicre et al. (2001). The fractions containing alkenones were concentrated, transferred to clean glass-vials and evaporated under nitrogen. Gas chromatographic analyses were performed on a Hewlett Packard 6890 gas chromatograph with flame ionization detector using a fused silica capillary column (Rxi-1ms, 50 m long, 0.32 mm internal diameter, 0.25 μm film thickness). Helium was used as a carrier gas. We have converted the alkenone index into temperature using the Prahl et al. (1988) calibration (see Supplementary Information Section 1.3).

Long chain diols were isolated by silica gel chromatography following the procedure of Rampen et al. (2012). Compound identification of the long chain diols was conducted using an Agilent 6890N gas chromatograph (GC) equipped with an Agilent 5975B mass selective (MS) detector in selective ion monitoring mode operated at 100

eV (EI Source). They were separated using a fused silica capillary column (ZB-5MS, 30 m long, 0.32 mm internal diameter, 0.25 μm film thickness). The relative abundance of long chain diols was measured using single ion monitoring of m/z 299, 313, 327, and 411.

2.4. Ice sheet/shelves simulations

2.4.1. General Circulation Model (GCM) set-up and simulations

Our RegCM3 experiments were initialised from GENESIS3 GCM simulations previously run at UMass Amherst (DeConto, et al., 2012; DeConto and Kowalewski unpublished). The GCM was run for 30 years to equilibrate, and then for a further 11 years to provide input (initial / boundary conditions) for the RegCM3 regional climate model. To provide appropriate input for RegCM3, GENESIS3 was tuned for orbital forcing, CO_2 levels, and ice sheet configuration representative of MIS31. Ice sheet configurations for Neogene interglacials were provided from model results from the Pollard and DeConto (2009) ice sheet model (forced w/ GENESIS3 as well).

2.4.2. Regional Climate Model (RCM) set-up and simulations

The 11 years -period described above allows for a one-year spinup for the RCM, followed by a ten years model evaluation period. GCM derived boundary conditions were continuously updated every 6 hours of RCM simulation, with fields being interpolated by the 'RegCM3_Polar' package onto the new model grid. No proxy data were used during this phase of climate model set up, but RegCM3 simulations were validated against (1) GCM performance conducted with GENESIS3, and (2) RegCM3 forced with NCEP/NCAR reanalysis. Reanalysis driven runs are for the 1990-1999 period using observed SST forcing while the Genesis-driven runs employ SST forcing from a slab ocean model.

285

286 ### 2.4.3 Ice Sheet Model (ISM) set-up and simulations

287 For our main experiments, we used climate model outputs from GCM experiments in
288 which the ice sheet configuration was similar to present, since our ice sheet model
289 experiments also start from a modern configuration. This avoids the circularity of
290 simulation WAIS collapse by imposing a climatology that has been produced under
291 conditions of a collapsed WAIS. We ran simulations with two different atmospheric
292 greenhouse gas concentrations (280 and 400 ppm CO_2) to quantify the sensitivity of
293 our results to different background climate states. The climatologies from the regional
294 climate model RegCM3_Polar simulations (RegCM3 adapted to Antarctica; Fig. S3)
295 were imposed at the beginning of each run and the ice sheet was allowed to freely
296 evolve to the new boundary conditions. Ice sheet experiments used the Parallel Ice
297 Sheet Model (PISM) version 0.6, whose dynamical core combines velocity solutions
298 of the shallow shelf and shallow ice approximations for the entire domain (see
299 Supplementary Information Section 2). We ran duplicate experiments both with, and
300 without, the sub-ice shelf grounding line melt interpolation scheme turned on. Once
301 afloat, we imposed two calving mechanisms – one based on horizontal strain rates
302 (Levermann et al., 2012), and another in which a simple minimum thickness criterion
303 (200m) must be satisfied. We ran experiments for two climate scenarios, reflecting
304 atmospheric CO_2 concentrations of 280 and 400 ppm, and for each of these, ran
305 duplicates with each of the two grounding-line parameterizations. All simulations
306 were run for 10000 years and were initialized from a thermally and dynamically
307 stable configuration used previously (Golledge, et al., 2015; 2017a; 2017b) which
308 closely resembles the present-day ice sheet (Fig. S4 panel a). Ice sheet configurations
309 after 5000 years for each of the experiments are shown in Figure S4.

3. Results

3.4. Early Pleistocene Southern Ocean sea surface temperatures

Our SST records were generated using the alkenone unsaturation proxy ($U^{k'}_{37}$ - Prahl et al., 1988) in the ice-free Antarctic zone (ODP Site 1094) and in the polar zone ODP Site 1101 and the Long Chain Diol Index (LDI – Rampen et al., 2012) at the IODP Site 1361 (Fig. 3). Two temperature proxies were used because although $U^{k'}_{37}$ is well-established, the calcareous nannofossils that produce alkenones (Marlowe et al., 1990; Beltran et al., 2007; 2011) are not always detectable in the coldest high latitude ocean regions. In contrast, the long chain diols used in the LDI index offer a good alternative as they are ubiquitous in the ocean, including at high latitudes (74°S) and LDI- and $U^{k'}_{37}$-derived SSTs record similar water depths and seasons (Rampen et al., 2012).

At ODP Site 1094, our record for the interval between 1.11 Ma and 0.95 Ma shows that the summer SSTs were on average 8.6 °C (between 5.3 °C and 10.8 °C), which is 3 °C warmer than today (Southern Hemisphere Summer months - Levitus, 1994; Fig. 3). This indicates sustained long-term elevated ocean surface temperatures in this sector of the Southern Ocean (Fig. 3A). At about 1.076 Ma, we identify a 10.8±1 °C temperature peak, i.e. 6 °C warmer than today, which we interpret as the MIS31 temperature optimum. Our data shows that during MIS31, SSTs closely track changes in Southern Hemisphere summer insolation with the warmest conditions reached during the highest Southern Hemisphere summer insolation maxima at 1.08 Ma (Laskar et al., 2004). We also observe large magnitude rapid temperature variations, e.g. 5.5 °C warming between 1082.69 ka and 1082.05 ka.

At ODP Site 1101 and IODP Site 1361, the age model and sampling resolution is

lower than at ODP Site 1094. However, at both sites, our data show that MIS31 corresponds to a summer SST increase of more than 5 °C compared to today (Levitus, 1994; Fig. 3A). The average SST through MIS31 at ODP Site 1101 is ~ 9.5 °C, peaking at about ~11 °C (1.069 Ma), which, is 7 °C warmer than the modern conditions. At IODP Site 1361, (the age model is less well constrained) the average surface water temperature during MIS31 was between 0 and 1°C, reaching a maximum value of 5 °C (6 °C warmer than today - Levitus, 1994). This result is in agreement with the Mg/Ca measurements on planktic foraminifera (Dunbar, 2012) and diatom based MIS31 temperature estimates (Scherer et al., 2008 and Scherer comm. pers.) from the Unit 3.1 at CRP-1B who suggests summer SSTs in the Ross Sea were warmer than today by 5-9°C.

Our paleotemperature reconstructions based on organic biomarkers, show that the surface ocean, south of 50 °S, warmed on average by 5 °C (± 1 to 2 °C) (Fig. 3 and 4), providing the first precise constraints on the maximum surface ocean temperature during MIS31.

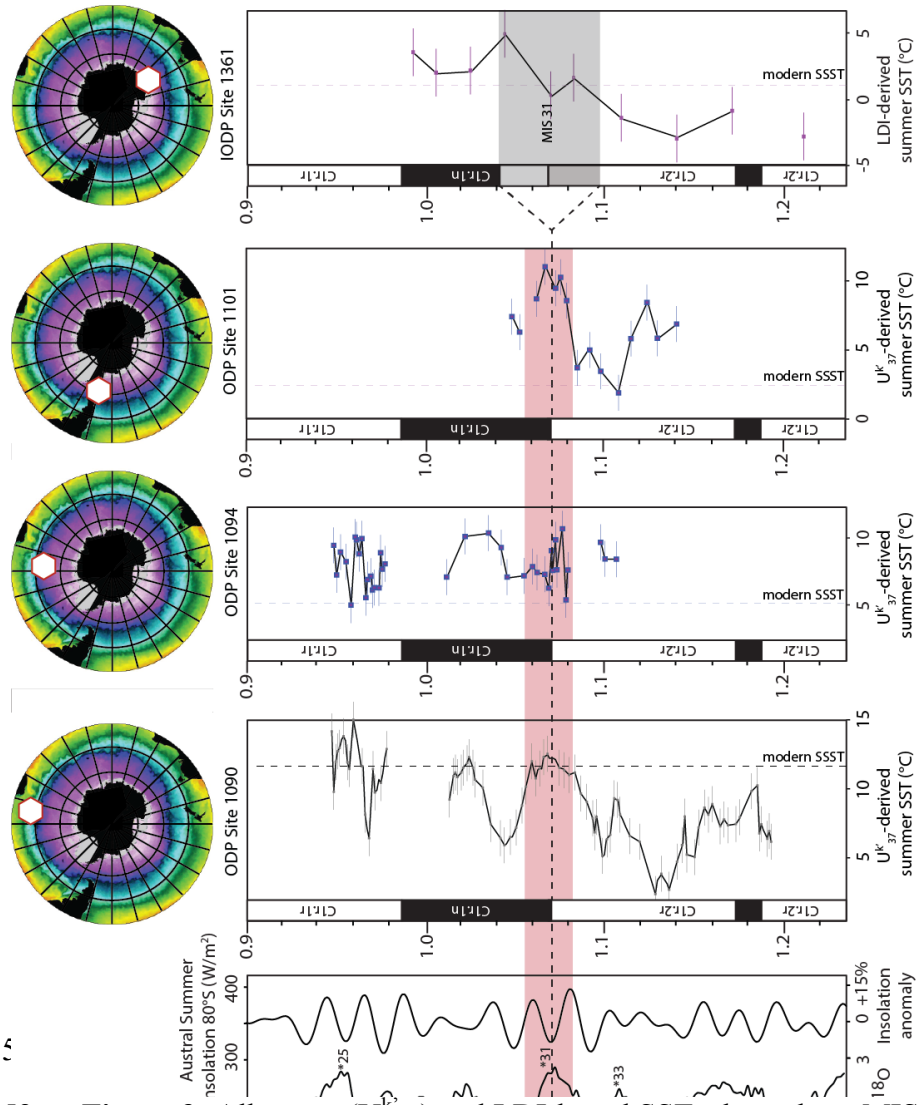

Figure 3: Alkenone ($U^{k'}_{37}$) and LDI-based SSTs throughout MIS31.
We show time series of deep-sea benthic $\delta^{18}O$ record (‰) (Lisiecki and Raymo, 2005), austral summer insolation at 80 °S and insolation anomaly relative to present (%increase relative to present; Laskar et al., 2004). Some of the MIS peaks are indicated with the symbol *. MIS31 interglacial duration is highlighted in red. The black dotted horizontal line shows the age of MIS31's peak (*31). Due to the uncertainties on the age model at Site 1361, MIS31 peak is highlighted in grey. Each map indicates the site locations. The error bars correspond to the error of each temperature proxy.
Summer southern hemisphere summer season which is here the average temperature for the months DJF

Our temperature record from ODP Site 1094 also indicate strong high-frequency variability within this warm period.

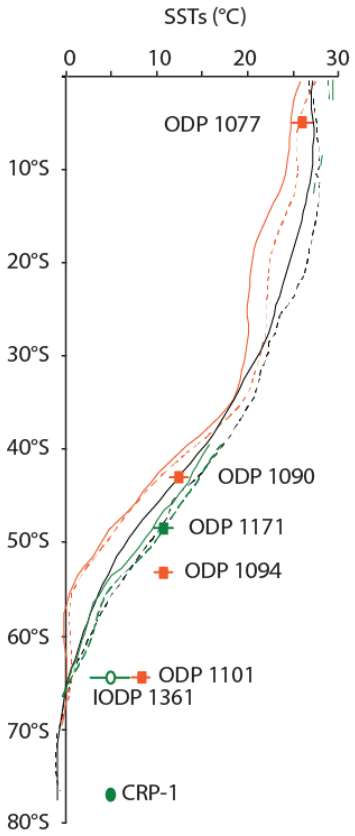

Figure 4: Comparison of the latitudinal sea surface temperature gradients during MIS31 warmth with modern conditions. MIS31 temperature data for Site ODP 1077 is from Schefus et al. (2004), for ODP Site 1171 from Beltran et al. (2016) and for CRP-1 from Dunbar (2012). The orange and green bars represent respectively the error bars for alkenone and LDI measurements.
Black dashed line: Modern Annual Southern Ocean SST - Green dashed line: Modern Annual Atlantic Ocean SST - Orange dashed line: Modern Annual Pacific Ocean SST - Green line: Modern Austral Summer Southern Ocean SST - Orange line: Modern Austral Summer Atlantic Ocean SST - Black line: Modern Austral Summer Pacific Ocean SST.

When comparing our high latitude records with the lower latitude alkenone-derived SSTs at the subantarctic ODP Site 1090 and the equatorial ODP Site 1077 (Schefus et al., 2004 - Fig. 4), we observe a significant polar amplification during MIS31, resulting in a reduced latitudinal SST gradient (Scherer et al., 2008; Martinez-Garcia et al., 2010; Dunbar, 2012; Beltran et al., 2016) of ~ -0.3 °C/ °latitude (Fig. 4).

3.2. Modelling the AIS during MIS 31

To investigate the degree of ice sheet retreat in relation to our SST records we conducted a suite of numerical simulations that use climate fields from a regional climate model (DeConto et al., 2012 - RCM, Supplementary Section 2). Our proxy data were critical to the simulations because they were the quality assurance that the simulations were capturing the correct magnitude of warming. We used the Parallel Ice Sheet-Model, which is an open source three-dimensional thermodynamic coupled ice sheet/ice-shelf model. Our RCM simulation represents a time slice reconstruction

rather than a transient prediction, but considers two atmospheric CO_2 concentration scenarios - 280ppm and 400ppm - so that the sensitivity of the ice sheet to atmospheric composition can be assessed (Supplementary Section 2.2). Using these two scenarios as inputs, we also then combined each one with either a conservative grounding line scheme (no SGm) or a more dynamic grounding line (SGm). Because our climate forcing is not transient, we were interested primarily in seeing whether significant ice sheet impacts could occur within relatively short time periods (centuries to a millennium) of warmth, since our proxy data indicate that such temperatures are not likely to have been sustained for the entire interglacial.

In all simulations, the WAIS melted within a few centuries (Fig. 5B, C, D, E and F) whereas the EAIS responded more slowly (Supplementary Section 2.3). The simulations revealed that regardless of the grounding line scenario and CO_2 forcing, no significant difference in the spatial extent of ice loss is observed after 5kyr (Fig. S4).

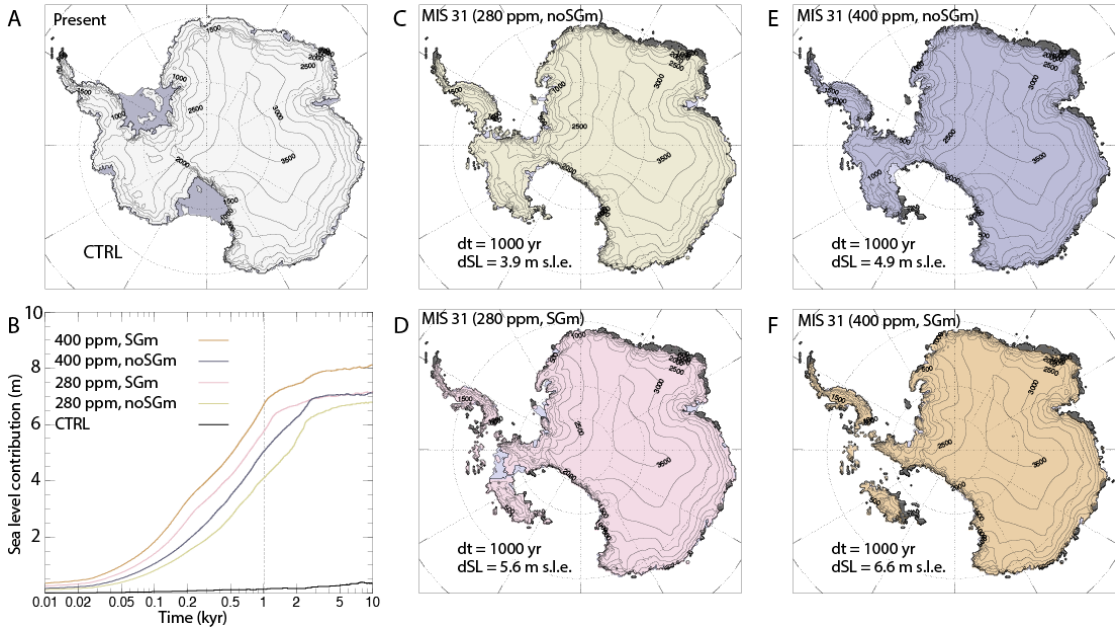

Figure 5: Snapshots of ice distribution for ice sheet experiment runs of 1000 years (dt). We present the results using a conservative groundling line behaviour (no SGm, C. and E.), a dynamic grounding line (SGm, D. and F.), each with two extreme CO_2 scenarios (280 ppm and 400 ppm). A. represents the modern ice distribution and B. is

the sea level contribution from ice melting through time. dSL is the sea level increase expressed in s.l.e (sea level equivalent).

Our results indicate that 2-m of sea-level rise from ice loss occur within a few centuries (Fig. 5B) and that persistent elevated SSTs would cause complete collapse of the WAIS, with additional thinning around the margins of the EAIS (i.e. the Wilkes Land basin, Weddell Sea, Aurora Basin).

4. Discussion and conclusions

Our temperature reconstructions indicate proximal ice margin summer SSTs of 4-5 °C in East and 9°C in West Antarctica (5-7 °C warmer than today) during MIS31, in agreement with Scherer et al (2008), Villa et al. (2008, 2012). Those temperatures are not compatible with the presence of a significant West Antarctic ice sheet (Joughin and Alley, 2011; Liu et al., 2015 - Fig. 5).

The causes of the MIS31 extreme warmth under pre-industrial atmospheric CO_2 conditions are still unclear. MIS31 interglacial coincides with a time of high obliquity and eccentricity, which led to strong high latitude austral summer insolation anomalies. How much of the ocean warming observed in our records can be attributed to the high summer insolation? Simulations of previous interglacials (Yin and Berger, 2012) showed that reduction of summer sea ice increases the sensitivity of southern high latitudes to solar radiation (Yin and Berger, 2012) resulting in warming of surface waters. According to Yin and Berger (2012), during interglacials with similar obliquity values as MIS31, increased insolation contributed to a maximum mean annual warming of only 0.5 °C of the high southern hemisphere latitudes. As a consequence, high insolation alone cannot account for the extreme ocean temperatures we observe around Antarctica during MIS31. We argue here that the exceptional warmth is the consequence of an increasingly stratified ocean due to freshwater input from ice loss (Golledge et al., 2014) rather than a trigger for ice loss.

426 Reduced surface ocean salinity is supported by the diatom assemblage composition at
427 CRP-1 with increased abundance of *Chaetoceros* spp. correlated to the insolation
428 maximum at 1.08 Ma (Scherer et al., 2008). The calcareous nannofossil assemblage
429 composition at ODP Site 1094 also support this hypothesis with a clear increase of
430 *Helicosphaera carteri* and *Syracosphaera* spp. (Flores and Sierro, 2007; Scherer et
431 al., 2008).
432 We suggest ice margin retreat was caused by circulation changes in Antarctic coastal
433 waters, as a result of changes in wind patterns (Gille et al., 2016). A poleward shift of
434 the Southern Hemisphere Westerly Winds (SHWW) is seen in the decrease of aeolian
435 dust in the Subantarctic Zone (Martinez-Garcia et al., 2010 - ODP Site 1090), raising
436 the possibility that a wind-induced subsurface warming at the Antarctic margin took
437 place during MIS31. In the modern ocean, cold Antarctic shelf waters are separated
438 from warmer Circumpolar Deep Water (CDW) further offshore by the Antarctic
439 Slope Front (ASF – Jacobs, 1991), a well-marked density front that is primarily
440 maintained through coastal downwelling induced by the prevailing coastal easterly
441 winds (Sverdrup, 1953). Ocean model simulations have demonstrated that a poleward
442 shift of the SHWW reduces the extent and strength of the coastal easterlies and can
443 produce strikethrough advective warming of subsurface waters at the Antarctic
444 margin, via a weakening of the ASF that allows CDW to intrude onto the shelf
445 (Schmidtko et al., 2014; Gille et al., 2016). Heat from the CDW would subsequently
446 trigger basal melting of the ice shelves (Dinniman et al., 2016). Additional
447 observational (Schmidtko et al., 2014; Dutrieux et al., 2014) and modelling evidence
448 (Thoma et al., 2008; Dinniman et al., 2012) also implicates the SHWW in regulating
449 poleward transport of warm CDW onto the Antarctic continental shelf in the modern-
450 day ocean, and it therefore seems plausible that this onshore CDW transport was

enhanced by poleward-intensified winds during MIS31 (Martinez-Garcia et al., 2010). Precise dynamics underlying such wind-driven CDW inflow however remain an area of active research (Gille et al., 2016).

We propose that the exceptional surface ocean warming during the MIS31 super-interglacial occurred in two steps (Fig. 6). [Step 1] The unusual MIS31 orbital configuration resulted in an extended period (~ 2000 years) of warm and long-lasting summer seasons that caused mild warming of Southern Ocean surface waters and the reduction of sea ice development or survival. Concomitantly, the prevailing Southern Hemisphere Westerly Winds and the easterly coastal winds migrated to the south (Fig. 6). The poleward shifted winds warmed the coastal waters, thus bringing heat southwards thereby initiating basal melting of ice shelves and the retreat of the marine-based grounding lines. Our numerical ice sheet model demonstrates that a 0.5 °C ocean warming at the ice margin for c. 200 years is sufficient to cause ice retreat and that most of it can occur in less than 2000 years. [Step 2] The surface warming in the coastal regions (9.5 °C at ODP Site 1101 and 5 °C at IODP Site 1361) could only take place after complete loss of the WAIS (Fig. 6) and would likely be amplified by ocean stratification feedbacks.

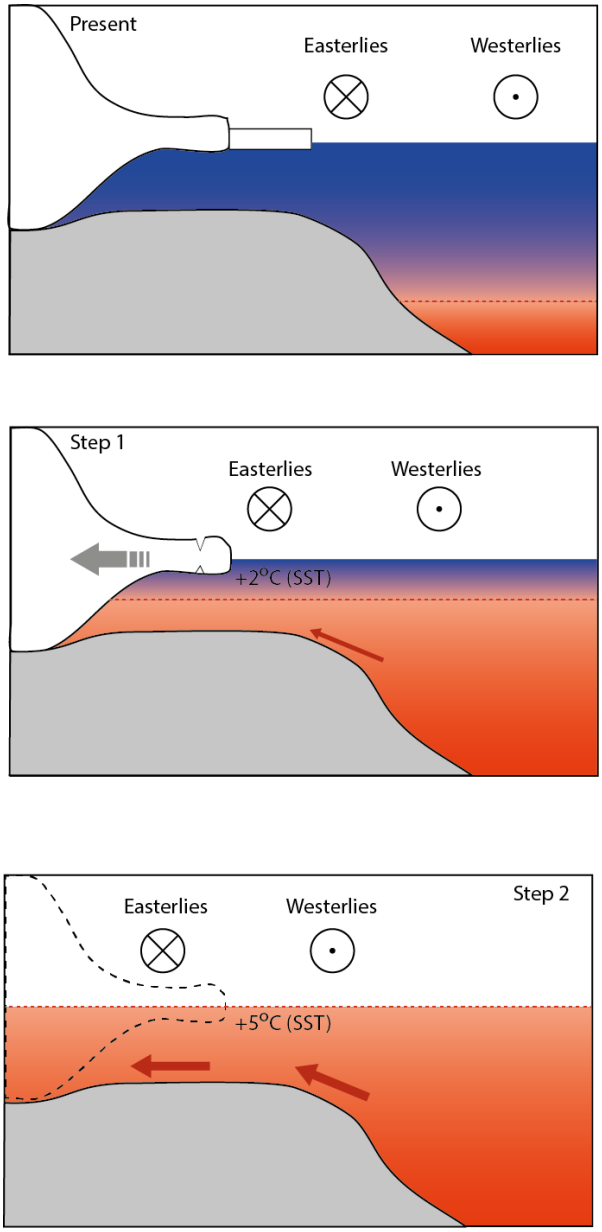

Figure 6: Schematic evolution of ice retreat during MIS31 in response to poleward wind shift and subsequent ocean warming. Step 1 shows the increased advection of warmer deep waters (red arrow, see Pedro et al., 2016), Step 2 represents the run over ice melting at the maximum of MIS31 warmth.

Our new data from the Antarctic sedimentary records demonstrate that a moderate surface ocean warming is sufficient to initiate a major West Antarctic Ice Sheet retreat. We also show that even after 10000 years of persistent elevated SSTs, marine basins of East Antarctica remain glaciated, with the majority of the EAIS sea-level contribution coming from coastal thinning around Dronning Maud Land. That the

479 marine basins of EAIS were not destabilized at MIS31 suggests that atmospheric
480 warming (as simulated in the RCM) at that time was insufficient to bring about
481 significant surface melting, thinning, and retreat from coastal pinning points
482 (Golledge et al., 2017b).
483 Future research should focus on further documenting high latitude Southern Ocean
484 SSTs using molecular thermometry to identify critical ocean temperatures that led to
485 major Antarctic ice retreats in the past under varying atmospheric CO_2 and orbital
486 conditions.
487

488 **Acknowledgments**
489 This project was funded by the French Institut National des Sciences de l'Univers and
490 the New Zealand Antarctic Research Institute contracts LEFE/IMAGO 2013, NZARI
491 2015-3 to Catherine Beltran and a University of Otago Research Grant to Christian
492 Ohneiser. The research used samples provided by the International Ocean Drilling
493 Program, which is sponsored by the US NSF and participating countries under
494 management of Joint Oceanographic Institutions. We are grateful to the International
495 Ocean Drilling Program curatorial staff at the Bremen Core Repository (BCR -
496 University of Bremen, Germany) and the Gulf Coast Repository (GCR - Texas A&M
497 University, College Station, Texas) for assistance with sample collection and
498 processing of sample requests.
499 We are grateful to Maria Rugenstein for providing climate model outputs. Nicholas R.
500 Golledge acknowledges support from the Royal Society Te Aparangi under contract
501 VUW1501.
502

References

Acton, G., Guyodo, Y., Brachfeld, S., 2012. Magnetostratigraphy of sediment drifts on the continental rise of West Antarctica (ODP Leg 178, Sites 1095, 1096 and 1101). Proceedings of the Ocean Drilling Program: Scientific Results 178, 1-61.

Barker, P.F., Camerlenghi, A., Acton, G.D., et al., 1999. Proc. ODP, Init. Repts. 178. http://www -odp.tamu.edu/publications/178_IR/178TOC.HTM.

Becquey, S. and Gersonde, R., 2002. Past hydrographic and climatic changes in the Subantarctic Zone - the Pleistocene record from ODP Site 1090. Palaeogeogr. Palaeoclimatol. Palaeoecol. 182, 221–239.

Beltran, C., de Rafélis, M., Minoletti, F., Renard, M., Sicre, M-A., Ezat, U., 2007. Coccolith $\delta^{18}O$ and alkenone records in Middle Pliocene orbitally controlled deposits: High-frequency temperature and salinity variations of sea surface water. Geochem. Geophys. Geosyst. 8. https://doi.org/10.1029/2006GC001483.

Beltran, C., Flores, J-A., Sicre, M-A. Baudin, F., Renard, M., de Rafélis, M., 2011. Long-chain alkenones in the Early Pliocene Sicilian sediments (Trubi Formation – Punta di Maiata section): implications for the alkenone paleothermometry. Palaeogeo. Palaeoclim., Palaeoeco. 308(3), 253-263. https://doi.org/10.1016/j.palaeo.2011.03.017.

Beltran, C., Ohneiser, C., Hageman, K.J., Scanlan, E., 2016. Evolution of the Southwestern Pacific surface waters during the Early Pleistocene. New Zealand Journal of Geology and Geophysics 59:4, 514-521. https://doi.org/10.1080/00288306.2016.1195756.

Bohaty, S., Scherer, R., Harwood, D.M., 1998. Quaternary diatom biostratigraphy and paleoenvironments of the CRP-1 drillcore, Ross Sea, Antarctica. Terra Antarctica 5, 431-453.

Channell, J., 2017. Cobb Mountain Subchron recorded at IODP Site U1306 (Eirik Drift, off SE Greenland). Geophysical Journal International 209(3), 1389–1397.

Channell, J. and Stoner, J., 2002. Plio-Pleistocene magnetic polarity stratigraphies and diagenetic magnetite dissolution at ODP Leg 177 Sites (1089, 1091, 1093 and 1094). Marine Micropaleontology 45(3-4), 269-290.

de Bar, M.W., Stolwijk, D.J., McManus, J.F., Sinninghe Damsté, J.S., Schouten, S., 2018. A Late Quaternary climate record based on long-chain diol proxies from the Chilean margin. Clim. Past 14, 1783–1803. https://doi.org/10.5194/cp-14-1783-2018.

DeConto, R.M., Pollard, D., Kowalewski, D., 2012. Modeling Antarctic ice sheet and climate variations during Marine Isotope Stage 31. Global and Planetary Change 88–89, 45–52.

Dinniman, M.S., Klinck, J.M., Hofmann, E.E., 2012. Sensitivity of Circumpolar Deep Water transport and ice shelf basal melt along the West Antarctic Peninsula to changes in the winds. Journal of Climate 25(4),799–4. https://doi.org/10.1175/JCLI-D-11-00307.1.

Dinniman, M.S., Asay-Davis, X.S., Galton-Fenzi, B.K., Holland, P.R., Jenkins, A., Timmermann, R., 2016. Modeling ice shelf/ocean interaction in Antarctica: A review. Oceanography 29(4), 144–153.

Dunbar, G.B., 2012. Mg/Ca sea surface temperatures during the Marine Isotope Stage 31 collapse of the Ross Ice Shelf. EGU General Assembly 2012, Vienna, Austria., 14473.

Dutrieux, P., De Rydt, J., Jenkins, A., Holland, P.R., Ha, H.K., Lee, S.H., Steig, E.J., Ding, Q., Abrahamsen, E.P., Schröder, M., 2014. Strong sensitivity of Pine Island

ice-shelf melting to climatic variability. Science 343,174-178. https://doi.org/10.1126/science.1244341.
Dutton, A. and Lambeck, K., 2012. Ice Volume and Sea Level During the Last Interglacial. Science 337. https://doi.org/10.1126/science.1205749.
Dutton, A., Carlson, A.E., Long, A.J., Milne, G.A., Clark, P.U., DeConto, R., Horton, B.P., Rahmstorf, S., Raymo, M.E., 2015. Sea-level rise due to polar ice-sheet mass loss during past warm periods. Science 349. https://doi.org/10.1126/science.aaa4019.
Expedition 318 Scientists, 2011. Site U1361. *In* Escutia, C., Brinkhuis, H., Klaus, A., and the Expedition 318 Scientists, *Proc. IODP,* 318: Tokyo (Integrated Ocean Drilling Program Management International, Inc.). https://doi.org/10.2204/iodp.proc.318.109.2011.
Gersonde, R. et al., 1999. Proceedings of the Ocean Drilling Program, 177 Initial reports. Proceeding of the Ocean Drilling Program 177. https://doi.org/10.2973/odp.proc.ir.177.1999.
Gille, S.T., McKee, D.C., Martinson, D.G., 2016. Temporal changes in the Antarctic Circumpolar Current: Implications for the Antarctic continental shelves. *Oceanography* 29(4), 96–105 https://doi.org/10.5670/oceanog.2016.102.
Golledge, N.R. Menviel, L., Carter, L., Fogwill, C.J., England, M.H., Cortese, G., Levy, R.H., 2014. Antarctic contribution to meltwater pulse 1A from reduced Southern Ocean overturning. Nature communications 5, 5107. https://doi.org/10.1038/ncomms6107.
Golledge, N.R., Kowalewski, D.E., Naish, T.R., Levy, R.H., Fogwill, C.J., Gasson, E.G.W., 2015. The multi-millenial Antarctic commitment to future sea-level rise. Nature 526. https://doi.org/10.1038/nature15706.
Golledge, N.R., Levy, R.H., McKay, R.M. Naish, T.R., 2017a. East Antarctic ice sheet most vulnerable to Weddell Sea warming. Geophys. Res. Lett. 44. https://doi.org/10.1002/2016GL072422.
Golledge, N.R., Thomas, Z.A., Levy, R.H., Gasson, E.G.W., Naish, T.R., McKay, R.M., Kowalewski, D.E., Fogwill, C.J., 2017b. Antarctic climate and ice sheet configuration during the early Pliocene interglacial at 4.23 Ma. Clim. Past 13, 1-17. https://doi.org/10.5194/cp–13-1-2017.
Hearty, P.J., Kindler, P., Cheng, H., Edwards, R.L., 1999. A +20m middle Pleistocene sea-level high-stand (Bermuda and the Bahamas) due to partial collapse of Antarctic ice. Geology 27, 375–378.
Hönisch, B., Hemming, N.G., Archer, D., Siddall, M., McManus, J.F., 2009. Atmospheric carbon dioxide concentration across the Mid-Pleistocene Transition. Science 324, 1551–1554. https://doi.org/10.1126/science.1171477.
Jacobs, S.S., 1991. On the nature and significance of the Antarctic Slope Front. Mar. Chem. 35, 9–24.
Jacobs, S.S., Hartmut, H., Doake, C.S.M., Jenkins, A., Frolich, R.M., 1992. Melting of ice shelves and the mass balance of Antarctica. J. Glaciol. 38, 375–387.
Joughin, I. and Alley, R.B., 2011. Stability of the West Antarctic ice sheet in a warming world. Nature Geosci. 4, 506–513.
Justino, F., Kucharski, F., Lindemann, D., Wilson, A., Stordal, F., 2019. A modified seasonal cycle during MIS31 super-interglacial favors stronger interannual ENSO and monsoon variability. Clim. Past 15, 735–749. https://doi.org/10.5194/cp-15-735-2019, 2019.

Kirschvink, J.L., 1980. The least-squares line and plane and the analysis of paleomagnetic data. Geophysical Journal of the Royal Astronomical Society 62(3), 699-718.

Laskar, J., Robutel, P., Joutel, F., Gastineau, M., Correia, A.C.M., Levrard B., 2004. A long-term numerical solution for the insolation quantities of the Earth. A. & A. 428, 261-285. https://doi.org/10.1051/0004-6361:20041335.

Levermann, A., Albrecht, T., Winkelmann, R., Martin, M. A., Haseloff, M., Joughin, I., 2012. Kinematic first-order calving law implies potential for abrupt ice-shelf retreat. Cryosphere 6, 273–286. https://doi.org/10.5194/tc-6-273-2012.

Levitus, S.E., 1994. Climatological atlas of the world ocean, NOAA Professional Paper 13, US Government Printing Office, Washington DC.

Lisiecki, L.E. and Raymo, M.E., 2015. A Pliocene-Pleistocene stack of 57 globally distributed benthic $\delta^{18}O$ records. Paleoceanography 20, PA1003. https://doi.org/10.1029/2004PA001071.

Liu, Y. Moore, J.C., Cheng, X., Gladstone, R.M., Bassis, J.N., Liu, H., Wen, J., Hui, F., 2015. Ocean-driven thinning enhances iceberg calving and retreat of Antarctic ice shelves. Proc. Natl Acad. Sci. USA 112, 3263–3268.

Lopes dos Santos, R.A., Spooner, M.I., Barrows, T.T., De Deckker, P., Sinninghe Damsté J.S., Schouten, S., 2013. Comparison of organic ($U^{K'}_{37}$, TEX^{H}_{86}, LDI) and faunal proxies (foraminiferal assemblages) for reconstruction of late Quaternary sea surface temperature variability from offshore southeastern Australia. Paleoceanography 28, 377-387. https://doi.org/10.1002/palo.20035

Lurcock, P.C. and Wilson, G.S., 2012. PuffinPlot: A versatile, user-friendly program for paleomagnetic analysis. Geochemistry, Geophysics, Geosystems 13(6).

Lüthi, D., Le Floch, M., Bereiter, B., Blunier, T., Barnola, J-M., Siegenthaler, U., Raynaud, D., Jouzel, J., Fischer, H., Kawamura, K., Stocker, T.F., 2008. High-resolution carbon dioxide concentration record 650,000-800,000 years before present. Nature 453, 379–382. https://doi.org/10.1038/nature06949.

Maiorano, P., Marino, M., Flores, J-A., 2009. The warm interglacial isotope Stage 31: evidences from the calcareous nannofossil assemblages at Site 1090 (Southern Atlantic). Marine Micropaleontology 71, 166–175.

Marlowe, I.T., Brassell, S.C., Eglinton, G., Green, J.C., 1990. Long-chain alkenones and alkyl alkenoates and the fossil coccolith record of marine sediments. Chem. Geol. 88, 349-375.

Martinez-Garcia, A., Rosell-Melé, A., McClymont, E.L., Gersonde, R., Haug, G.H., 2010. Subpolar Link to the Emergence of the Modern Equatorial Pacific Cold Tongue. Science 328, 1550-1553. https://doi.org/ 10.1126/Science.1184480**.**

McKay, R.M. Naish, T., Powell, R., Barrett, P., Talarico, F., Kyle, P., Monien, D., Kuhn, G., Jackolski, C., Williams, T., 2012. Pleistocene variability of Antarctic Ice Sheet extent in the Ross Embayment. Quaternary Science Reviews 34, 93-112.

Orsi, A.H., Whitworth, T., Nowlin, W.D., 1995. On the meridional extent and fronts of the Antarctic Circumpolar Current. Deep-Sea Res. I 42, 641–673.

Pedro, J.B., Martin, T., Steig, E.J., Jochum, M., Park, W., Rasmussen, S.O., 2016. Southern Ocean deep convection as a driver of Antarctic warming events. Geophysical Research Letters 43, 2192-2199.

Pollard, D. and DeConto, R.M., 2009. Modeling West Antarctic Ice Sheet growth and collapse through the last 5 million years. Nature 458, 329–332.

Prahl, F.G., Muehlhausen, L.A., Zahnle, D.L., 1988. Further evaluation of long-chain alkenones as indicators of paleoceanographic conditions. Geochim. Cosmochim. Acta 52, 2303-2310.

Rampen, S.W., Willmott, V., Kim, J-H., E. Uliana, Mollenhauer, G., Schefuß, E., Sinninghe Damsté, J.S., Schouten, S., 2012. Long chain 1,13- and 1,15-diols as a potential proxy for palaeotemperature reconstruction. Geochimica et Cosmochimica Acta 84, 204–216.

Raymo, M.E., Lisiecki, L., Nisancioglu, K., 2006. Plio-Pleistocene ice volume, Antarctic climate and the global $\delta^{18}O$ record. Science 313, 492-495.

Schefuß, E., Sinninghe Damste, J.S.S., Jansen, J.H.F., 2004. Forcing of tropical Atlantic sea surface temperatures during the mid-Pleistocene transition. Paleoceanography 19. https://doi.org/10.1029/2003PA000892.

Scherer, R.P., Harwood, D.M., Taviani, M., Bohaty, S.M., Roberts, A.P., 2003. Marine Isotope Stage 31 (1.07 Ma): an extreme interglacial in the Antarctic nearshore zone. Geophys. Res. Abstr. 5, 11710.

Scherer, R.P., Bohaty, S.M., Dunbar, R.B., Esper, O., Flores, J-A., Gersonde, R., Harwood, D.M., Roberts, A.P., Taviani, M., 2008. Antarctic records of precession-paced insolation-driven warming during early Pleistocene Marine Isotope Stage 31. Geophys. Res. Letters 35, L03505. https://doi.org/10.1029/2007GL032254.

Schmidtko, S., Heywood, K.J., Thompson, A.F., Aoki, S., 2014. Multidecadal warming of Antarctic waters. Science 346, 1227-1231.

Schneider-Mor, A., Yam, R., Bianchi, C., Kunz-Pirrung, M., Gersonde, R., Shemesh, A., 2008. Nutrient regime at the siliceous belt of the Atlantic sector of the Southern Ocean during the past 660ka. Paleoceanography 23, PA3217. https://doi.org/10.1029/2007PA001466.

Sicre, M.A., Ternois, Y., Paterne, M., Martinez, P., Bertrand, P., 2001. Climatic changes in the upwelling region off Cap Blanc, NW Africa, over the last 70 kyrs, a multi-biomarker approach. Organic Geochemistry 32, 981-990.

Sverdrup, H., 1953. The currents off the coast of Queen Maude Land. Norw. J. Geogr. 14, 1–4.

Tauxe, L., Stickley, C.E., Sugisaki, S., Bijl, P.K., Bohaty, S.M., Brinkhuis, H., Escutia, C., Flores, J-A., Houben, A.J.P., Iwai, M., Jiménez-Espejo, F., McKay, R., Passchier, S., Pross, J., Riesselman, C.R., Röhl, U., Sangiorgi, F., Welsh, K., Klaus, A., Fehr, A., Bendle, J.A.P., Dunbar, R., Gonzàlez, J., Hayden, T., Katsuki, K., Olney, M.P., Pekar, S.F., Shrivastava, P.K., van de Flierdt, T., Williams, T., Yamane, M., 2012. Chronostratigraphic framework for the IODP Expedition 318 cores from the Wilkes Land Margin: constraints for paleoceanographic reconstruction. Paleoceanography 27.

Teitler, L., Florindo, F., Warnke, D.A., Filippelli, G.M., Kupp, G., Taylor, B., 2015. Antarctic Ice Sheet response to a long warm interval across Marine Isotope Stage 31: A cross-latitudinal study of iceberg-rafted debris. Earth and planetary science letters 409, 109-119.

Thoma, M., Jenkins, A., Holland, D., Jacobs, S., 2008. Modeling Circumpolar Deep Water intrusions on the Amundsen Sea continental shelf. Geophysical Research Letters 35, L18602. https://doi.org/ 10.1029/2008GL034939.

Villa, G. and Wise, S.W., 1998. Quaternary Calcareous nannofossil from the Antarctic region. Terra Antarctica 5 (3), 479–484.

Villa, G., Lupi, C., Cobianchi, M., Florindo, F., Pekar, S.F., 2008. A Pleistocene warming event at 1 Ma in Prydz Bay, East Antarctica: Evidence from ODP Site 1165. Palaeogeo. Palaeoclim., Palaeoeco. https://doi.org/10.1016/j.palaeo.2007.08.017.

Villa, G., Persico, D., Sherwood, W.W., Gadaleta, A., 2012. Calcareous nannofossil evidence for Marine Isotope Stage 31 (1 Ma) in Core AND-1B, ANDRILL

McMurdo Ice Shelf Project (Antarctica). Global and Planetary Change. https://doi.org/10.1016/j.gloplacha.2009.12.003.

Winter, D., Sjunneskog, C., Scherer, R., Maffioli, P., Riesselman, C., Harwood, D., 2010. Pliocene-Pleistocene diatom biostratigraphy of nearshore Antarctica from the AND- 1B drillcore, McMurdo Sound. Global and Planetary Change. https://doi.org/10.1016/j.gloplacha.2010.04.004.

Yin, Q.Z. and Berger, A., 2012. Individual contribution of insolation and CO_2 to the interglacial climates of the past 800,000 years. Clim. Dyn. 38, 709-724.

Supplementary Information for:

Southern Ocean temperature records and ice-sheet models demonstrate rapid Antarctic ice sheet retreat under low atmospheric CO_2 during Marine Isotope Stage 31.

*Beltran Catherine[1], Golledge Nicholas R.[2,3], Ohneiser Christian[4], Kowalewski Douglas E.[5], Sicre Marie-Alexandrine[6], Hageman Kimberly J.[7], Smith Robert[1], Wilson Gary S.[1], Mainié François[6].

Corresponding author: Catherine Beltran
Email: catherine.beltran@otago.ac.nz

1. Department of Marine Science, University of Otago, PO Box 56, Dunedin 9054, New Zealand
2. Antarctic Research Centre, Victoria University of Wellington, Wellington 6140, New Zealand
3. GNS Science, Avalon, Lower Hutt 5011, New Zealand
4. Department of Geology, University of Otago, PO Box 56, Dunedin 9054, New Zealand
5. Department of Earth, Environment, and Physics, Worcester State University, Worcester, Massachusetts 01602, USA
6. Sorbonne Universités (UPMC, Univ. Paris 06)-CNRS-IRD-MNHN, LOCEAN Laboratory, 4 Place Jussieu, F-75005 Paris, France.
7. Department of Chemistry, University of Otago, PO Box 56, Dunedin 9054, New Zealand

738 **Supplementary Information**

739 **Table of Contents**

740

741

742

743

744

745

746

Section 1: Sea surface temperature proxies

Climate simulations require unambiguous, continuous, and well-dated SST records to determine changes in latitudinal heat transport. Despite the emergence of new and well calibrated paleotemperature proxies based on diatom morphometry (e.g. Allen, 2014; Kloster et al., 2018; Shukla and Romero, 2018), the few available high latitude Southern Ocean SST reconstructions for MIS31 were either derived from 1) proxies based on calcareous nannofossil and planktonic foraminifera assemblage compositions that tend to be less reliable at high latitudes where the species diversity is low 2) diatom assemblages which composition reflect not only temperatures but also environmental parameters such as sea ice, nutrients and light etc… or 3) uncorrelated temperature proxies possibly reflecting temperatures of different water masses and/or seasons, which adds significant uncertainties to climate reconstructions. The lack of accurate and consistent SSTs for the Sub-Antarctic and Antarctic zones of the Southern Ocean during MIS31 greatly restricts our ability to precisely quantify the global latitudinal ocean heat transfer and subsequent sub-ice ocean heat flux, impacting our ability to simulate the AIS response to ocean temperature changes. To reconstruct the most continuous latitudinal record of the SSTs during the MIS31 super-interglacial along a transect from Sub-Antarctic to Antarctic water bodies in the Atlantic sector of the Southern Ocean, we used two complementary organic geochemical proxies for SSTs: the alkenone unsaturation ratio ($U^{k'}_{37}$, Prahl et al., 1988) and the Long Chain Diol Index (LDI, Rampen et al., 2012).

1.1. Alkenone thermometry

The C_{37} alkenone unsaturation index ($U^{k'}_{37}$; Eq. 1) is a robust proxy for SST, providing surface ocean temperature reconstructions with a precision of +/-1.2 °C (Sikes and Volkman, 1993; Muller et al., 1998; Conte et al., 2006).

772
$$U^{k'}_{37} = \frac{[C_{37:2}]}{[C_{37:2}]]+ [C_{37:3}]} \qquad \text{Eq. 1}$$
773

774 Global core-top studies demonstrate that $U^{k'}_{37}$ correlates best with mean annual
775 temperatures at 0–10 m water depth range (Conte et al., 1993) and there is little
776 evidence that the SST signal is affected by other environmental parameters such as
777 productivity or salinity.
778 Previous studies (Sikes and Volkman, 1993; Conte et al., 2006;) showed that south of
779 40°S in the Pacific and Atlantic sectors of the Southern Ocean, alkenone production is
780 limited to late spring-summer. As both ODP Sites 1090 and 1094 chosen in our study
781 were drilled south of the subtropical front, the $U^{k'}_{37}$-derived SST reconstructions are
782 likely to reflect the mixed-layer conditions during the warmest months of the year.
783 *1.2. Long chain Diol Index thermometry for IODP Site U1361*
784 The Long-chain diol index (LDI; Eq. 2) is defined as:
785
$$LDI = \frac{[C_{30}1,15\text{-diol}]}{[C_{28}1,13\text{-diol}]+[C_{30}1,13\text{-diol}]+ [C_{30}1,15\text{-diol}]} \qquad \text{Eq. 2}$$
786

787 Core top studies indicate that the LDI index is linearly correlated to SSTs (+/-2°C) in
788 a range of temperatures from -3°C to 27°C (Eq. 3) with salinity and nutrient
789 conditions having little to no influence (Rampen et al., 2002).
790
$$LDI = 0.033 \times SST + 0.095 \qquad \text{Eq. 3}$$

791 *1.3. Alkenone Calibration*
792 Most alkenone-derived SST reconstructions use the calibration of Prahl et al.(1988)
793 based on the empirical linear relationship between $U^{k'}_{37}$ and SST obtained from
794 laboratory cultures. However, several studies show that the $U^{k'}_{37}$ measured in
795 particulate matter of surface waters disagree with this calibration (Prahl et al.,1988).
796 These observations led to the development of alternate calibrations either global such

as the polynomial $U^{k'}_{37}$ -SST relationship of Conte et al. (2006) or region-specific (Muller et al., 1998; Sikes and Volkman, 1993).

To select the most accurate $U^{k'}_{37}$ calibration, we have extended the ODP Site 1094 sampling (Fig. S1) to cover the long term evolution of SSTs until today.

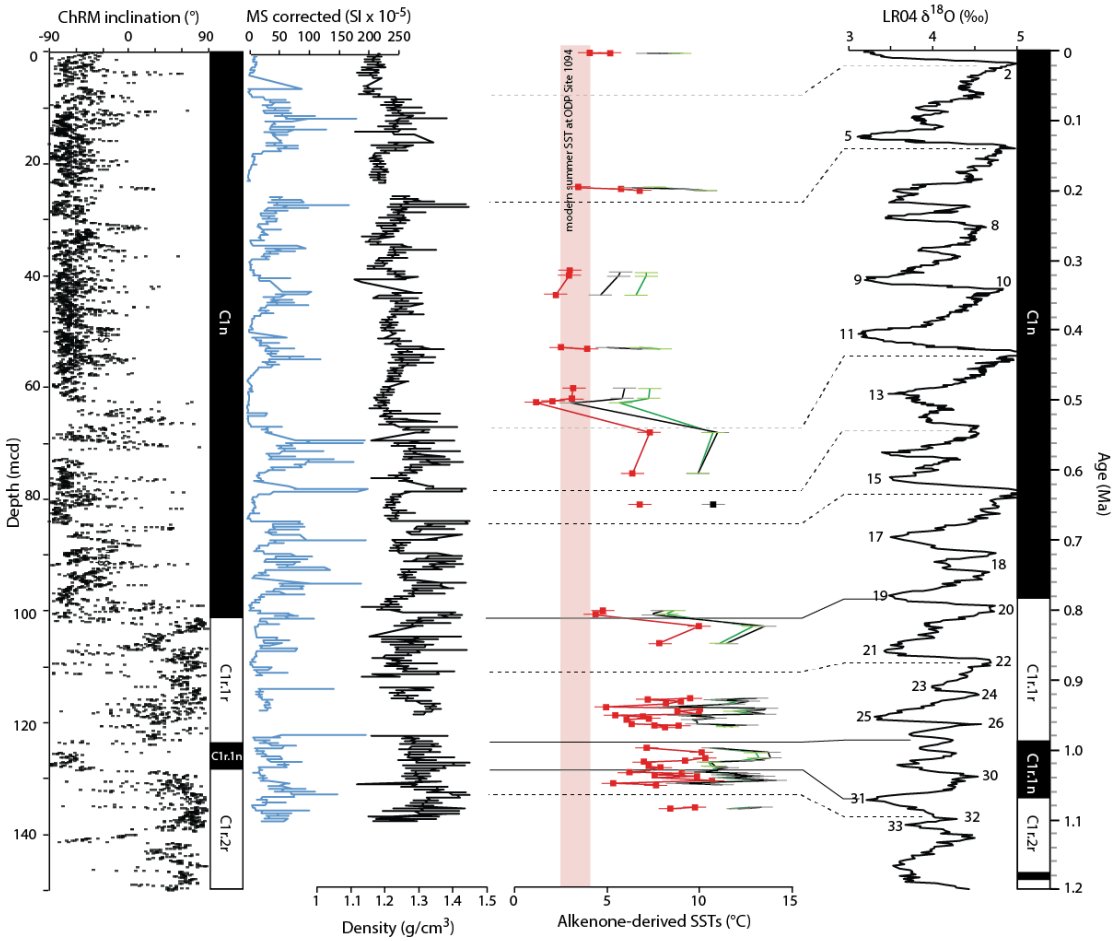

Fig. S1. *Long term evolution of the alkenone-derived sea surface temperatures at ODP Site 1094 using three different calibrations : Prahl et al. (1988) in red; Sikes and Volkman (1993) in green; Conte et al. (2006) in black. Our additional low resolution dataset shows that the Prahl et al.(1988) calibration leads to SSTs that are similar to the modern ones at the same location.*

When comparing the core top SSTs with the Levitus monthly modern SSTs it appears that the Prahl et al. (1988) calibration leads to values that are consistent with the modern February SSTs at the same location (Fig. S1). We have thus converted the alkenone index into temperature using the Prahl et al. (1988) calibration.

Section 2: Ice sheet/shelves simulations

2.1. Global Climate Modelling.

The relationship between air and ocean temperatures under different CO_2 conditions evolves through time (Rugenstein et al., 2016), such that in Antarctica, short-term (< 100 year) sea-surface temperature anomalies are considerably less than the equilibrium state (Fig. S2 below). When attempting to infer an atmospheric warming from our oceanic proxy data, therefore, we conservatively assume that the ocean / atmosphere warming has achieved balance (taking c. 1000 years), and thus mean annual sea temperature anomalies are likely to be c. 2.5 times the inferred mean annual air temperature anomaly (SST to air ratio of 0.4, Fig. S2).

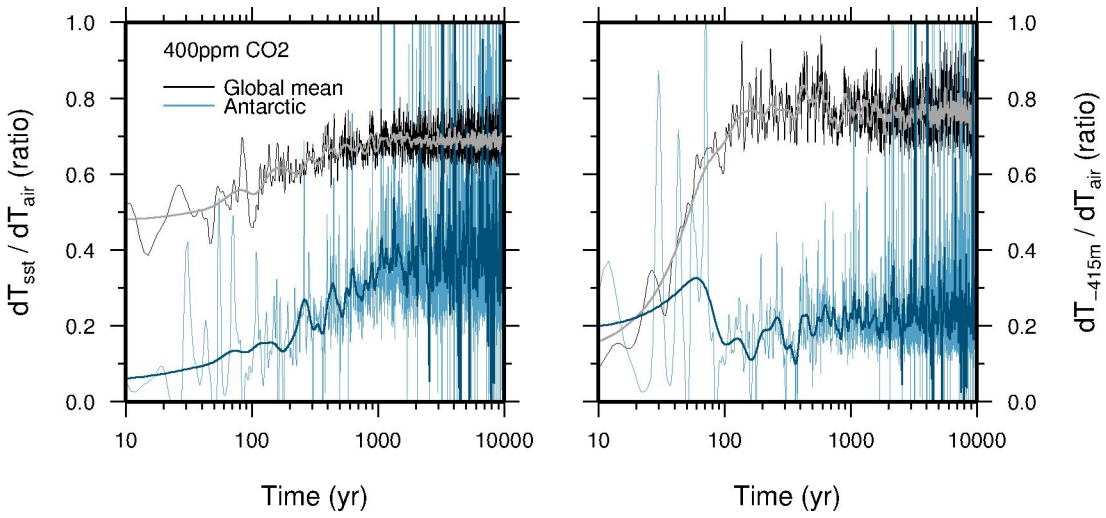

Fig. S2. *Evolution of the relationship between mean annual surface air temperature anomaly and that of the sea surface (left) and ocean at 415 m depth (right) for Antarctica, compared to the global mean (Rugenstein et al., 2016). An equilibrium SST to air ratio of 0.4 implies a 2.5 times greater air temperature anomaly than that felt by the sea surface.*

2.2. Regional Climate Modelling

Paleoclimate simulations were run using RegCM3_Polar. The regional climate model, RegCM3, was adapted to Antarctica (RegCM3_Polar) centered on the South Pole for Antarctic reconstructions. Boundary conditions for the regional model were taken from the library of existing GCM Pliocene simulations (GENESIS v. 3.0.; Pollard and DeConto, 2009). Simulations varied greenhouse gas, orbital, sea ice and SST

conditions; changes in environmental conditions were prescribed in both the RCM and GCM. The boundary forcing from GENESIS GCM was interpolated horizontally and vertically to the RegCM3_Polar grid and topography and was applied at 6-hour intervals for both 40km and 80km horizontal resolution regional climate simulations. Regional climate simulations were run using existing ice configuration and a MIS31 modeled ice sheet configuration imported from the Pollard and DeConto ice sheet / shelf model output (Pollard and DeConto, 2009).

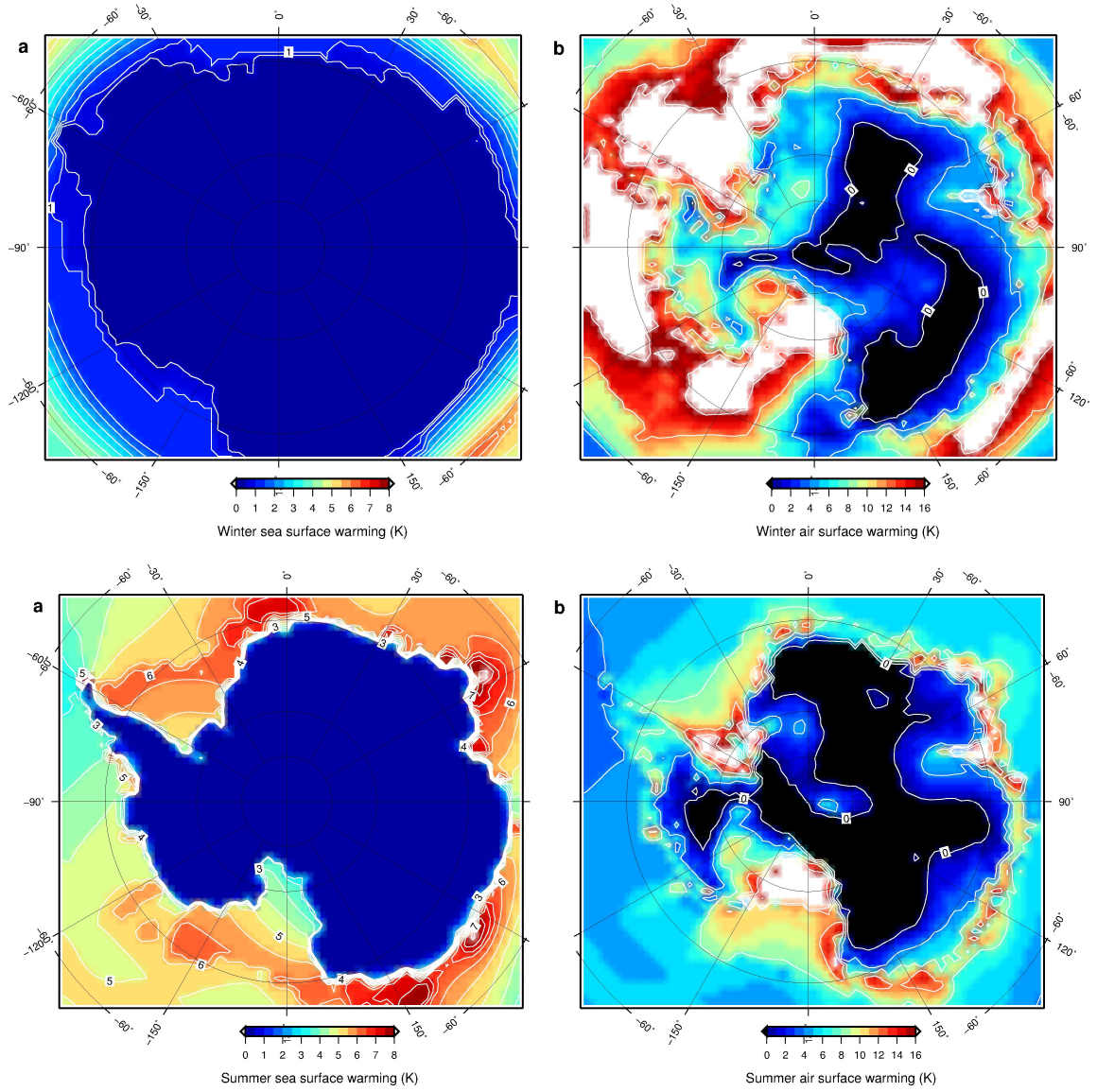

Fig. S3. *Seasonal climatologies for Antarctica during MIS31, as simulated by the Regional Climate Model, as anomalies from present-day.*

2.3. Ice Sheet Modelling

For our ice sheet experiments we use the climatologies from the RCM simulations (Fig. S3) as anomalies to present-day air temperature and precipitation fields (Lenaerts et al., 2012), in the same manner as employed previously (Golledge et al., 2017a). We use monthly climate fields in order to capture the high-latitude changes in seasonality brought about by the different orbital configuration of MIS31, compared to present. A positive-degree day model translates temperatures above freezing into surface melt, of which a proportion (60%) is retained in the snowpack through percolation refreezing processes. This value is difficult to constrain precisely (Kuipers Munneke et al., 2011) but here we use a constant value for both our control and our perturbation experiments, thus differences in the results are not likely to arise from errors in this parameterisation.

We use the Parallel Ice Sheet Model (PISM) version 0.6. Fast flow of grounded ice is facilitated by the plastic failure of subglacial sediments that arises as a consequence of an initially prescribed till friction angle, representing sediment strength, and its saturation state, which evolves dynamically in concert with the thermal properties of the basal layer of overlying ice. Thus where ice reaches sufficient thickness to allow basal melting to occur, meltwater begins to weaken the substrate until driving stresses exceed the evolving cohesiveness of the till. Failure of the substrate and the concomitant acceleration of overlying ice obeys a pseudo-plastic law (Schoof, 2006; Bueler and Brown, 2009), such that small increments of stress above the shear strength of the substrate lead to an increasing velocity response that ultimately thins the ice, reducing its driving stress and leading to deceleration of the ice. The cyclic

870 behaviour of ice streams that occurs as a consequence of this mechanism is described
871 in more detail elsewhere (Van Pelt and Oerlemans, 20120. PISM employs a sub-grid
872 grounding line scheme (Feldmann et al., 2014) in which sub-ice shelf melt may be
873 interpolated across the grounded-floating ice junction, or not. The former approach
874 tends to accelerate ice sheet retreat in marine basins, whereas the latter produces a
875 slower response (Golledge et al., 2015). Equilibrium states tend to differ less between
876 the two approaches than do retreat rates, however. For completeness, we run duplicate
877 experiments both with, and without, the sub-ice shelf grounding line melt
878 interpolation scheme turned on. Once afloat, we impose two calving mechanisms –
879 one based on horizontal strain rates (Levermann et al., 2012), and another in which a
880 simple minimum thickness criterion (200m) must be satisfied.
881 With the model setup described above, we undertook a series of simulations to
882 explore the range of likely ice sheet responses to MIS31 climate states as simulated by
883 the RCM. We ran experiments for two climate scenarios, reflecting atmospheric CO_2
884 concentrations of 280 and 400 ppm, and for each of these ran duplicates with each of
885 the two grounding line parameterisations described above. We also ran a control
886 experiment in which a present-day climate field was maintained throughout. All
887 simulations were run for 10000 years and were initialised from a thermally and
888 dynamically stable configuration used previously (Golledge et al., 2015; Golledge et
889 al., 2017a; 2017b) which closely resembles the present-day ice sheet (Fig. S4 panel a).
890 RCM-derived climatologies were imposed at the beginning of each run and the ice
891 sheet was allowed to freely evolve to the new boundary conditions. Ice sheet
892 configurations after 5000 years for each of the experiments are shown in Figure S4.

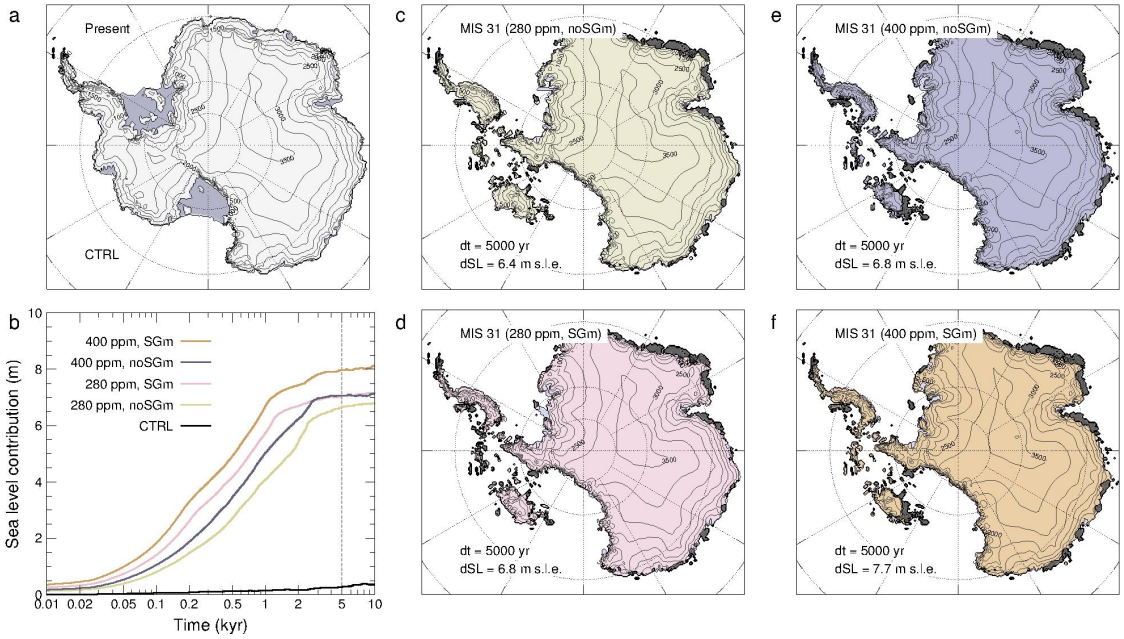

Fig. S4. *Ice sheet geometry and contribution to global sea level after 5000 years of simulated MIS31 climates, using either 280 ppm or 400 ppm atmospheric CO_2, and with one of two different grounding-line schemes (noSGm, SGm; see text for details). Note the rapid response of the ice sheet under all scenarios (panel b), corresponding to the collapse timescale of WAIS.*

Timeseries data illustrate that mass loss more-or-less stabilises after approximately 5000 years in most cases. In all MIS31 experiments, WAIS is lost relatively rapidly (first 1-2 millennia), with subsequent mass loss (from EAIS) taking place more slowly.

References:

Allen, C., 2014. Proxy development: A new facet of morphological diversity in the marine diatom Eucampia antarctica (Castracane) Mangin. Journal of Micropalaeontology 33, 131-142. https://doi.org/10.1144/jmpaleo2013-025.

Bueler, E. and Brown, J., 2009. Shallow shelf approximation as a "sliding law" in a thermomechanically coupled ice sheet model. Journal of Geophysical Research 114, F03008.

Conte, M.H. and Eglinton, G., 1993. Alkenone and alkenoate distributions within the euphotic zone of the eastern North Atlantic: correlation with production temperature. Deep-Sea Research 40, 1935-1961.

Conte, M.H., Sicre, M-A., Ruhlemann, C., Weber, J.C., Schulte, S., Schulz-Bull, D., Blanz, T., 2006. Global calibration of the alkenone unsaturation index $U^{k'}_{37}$ with surface water production temperature and a comparison of the coretop integrated production temperatures recorded by $U^{k'}_{37}$ with overlying sea surface temperatures. Geochemistry, Geophysics, Geosystems 72, 1–22.

Feldmann, J., Albrecht, T., Khroulev, C., Pattyn, F., Levermann, A., 2014. Resolution-dependent performance of grounding line motion in a shallow model compared to a full-Stokes model according to the MISMIP3d intercomparison. J. Glaciol. 60, 353–360.

Golledge, N.R., Kowalewski, D.E., Naish, T.R., Levy, R.H., Fogwill, C.J., Gasson, E.G.W., 2015. The multi-millenial Antarctic commitment to future sea-level rise. Nature 526. https://doi.org/10.1038/nature15706.

Golledge, N.R., Levy, R.H., McKay, R.M. Naish, T.R., 2017a. East Antarctic ice sheet most vulnerable to Weddell Sea warming. Geophys. Res. Lett. 44. https://doi.org/10.1002/2016GL072422.

Golledge, N.R., Thomas, Z.A., Levy, R.H., Gasson, E.G.W., Naish, T.R., McKay, R.M., Kowalewski, D.E., Fogwill, C.J., 2017b. Antarctic climate and ice sheet configuration during the early Pliocene interglacial at 4.23 Ma. Clim. Past 13, 1-17. https://doi.org/10.5194/cp–13-1-2017.

Kloster, M., Kauer, G., Esper, O., Fuchs, N., Beszteri, B., 2018. Morphometry of the diatom *Fragilariopsis kerguelensis* from Southern Ocean sediment: High-throughput measurements show second morphotype occurring during glacials. Marine Micropal. 143, 70-79. https://doi.org/10.1016/j.marmicro.2018.07.002.

Kuipers Munneke, P., van den Broeke, M.R., Lenaerts, J.T.M., Flanner, M.G., Gardner, A.S., van de Berg, W.J., 2011. A new albedo parameterization for use in climate models over the Antarctic ice sheet. Journal of Geophysical Research 116, D05114. https://doi.org/10.1029/2010JD015113.

Lenaerts, J., van den Broeke, M., van de Berg, W., van Meijgaard, E., Munneke, P., 2012. A new high-resolution surface mass balance map of Antarctica (1979–2010) based on regional atmospheric climate modelling. Geophysical Research Letters 39, L04501.

Levermann, A., Albrecht, T., Winkelmann, R., Martin, M. A., Haseloff, M., Joughin, I., 2012. Kinematic first-order calving law implies potential for abrupt ice-shelf retreat. Cryosphere 6, 273–286. https://doi.org/10.5194/tc-6-273-2012.

Muller, P.J., Kirst, G., Ruhland, G., Von Storch, I., Rosell-Mele, A., 1998. Calibration of the alkenone paleotemperature index $U^{k'}_{37}$ based on core-tops from the eastern South Atlantic and the global ocean (60°N-60°S). Geochimica et Cosmochimica Acta 62, 1757–1772.

Pollard, D. and DeConto, R.M., 2009. Modeling West Antarctic Ice Sheet growth and collapse through the last 5 million years. Nature 458, 329–332.

Prahl, F.G., Muehlhausen, L.A., Zahnle, D.L., 1988. Further evaluation of long-chain alkenones as indicators of paleoceanographic conditions. Geochim. Cosmochim. Acta 52, 2303-2310.

Rampen, S.W., Willmott, V., Kim, J-H., E. Uliana, Mollenhauer, G., Schefuß, E., Sinninghe Damsté, J.S., Schouten, S., 2012. Long chain 1,13- and 1,15-diols as a potential proxy for palaeotemperature reconstruction. Geochimica et Cosmochimica Acta 84, 204–216.

Rugenstein, M.A.A., Sedláček, J., Knutti, R., 2016. Nonlinearities in patterns of long-term ocean warming. Geophysical Research Letters 43, 3380–3388. https://doi.org/10.1002/2016GL068041.

Schoof, C.A., 2006. Variational approach to ice stream flow. J. Fluid Mech., 556, 227–251.

Shukla, S.K. and Romero, O.E., 2018. **Glacial valve size variation of the Southern Ocean diatom** *Fragilariopsis kerguelensis* **preserved in the Benguela Upwelling System, southeastern Atlantic**. Palaeogeogr. Palaeoclimatol. Palaeoecol. 499, 112-122. https://doi.org/10.1016/j.palaeo.2018.03.023.

Sikes, E.L. and Volkman, J.K., 1993. Calibration of alkenone unsaturation ratios ($U^{k'}_{37}$) for paleotemperature estimation in cold polar waters. Geochimistry et Cosmochimica Acta 57, 1883-1889.

Van Pelt, W.J.J. and Oerlemans, J., 2012. Numerical simulations of cyclic behaviour in the Parallel Ice Sheet Model (PISM). Journal of Glaciology 58, 347-360.